Int J Earth Sci (Geol Rundsch) (2017) 106:1619–1630
DOI 10.1007/s00531-016-1374-4

ORIGINAL PAPER

Three-dimensional structure and evolution of an asymmetric pull-apart basin

Amir Sagy[1] · **Yariv Hamiel**[1]

Received: 22 March 2016 / Accepted: 4 July 2016 / Published online: 19 July 2016

Abstract The structure of a ~250-m-long asymmetrical pull-apart basin developed in carbonate rocks at the Galilee heights, Israel, is herein analyzed. The reconstruction of the basin geometry is based on detailed mapping and LiDAR measurements of fault scarps. The architecture of faults is then used as a boundary condition for calculating the stress pattern in the vicinity of the basin, using a dislocation model. The basin is found to be an asymmetrical V-shaped structure bordered by two longitudinal oblique right-lateral strike–slip faults. The strike of one of the faults is bent at the eastern edge of the basin, generating a transverse boundary fault which joins the second boundary fault orthogonally. The overall lateral displacement is smaller than the basin length, and no transverse or diagonal fault is observed in the western end of the basin. The deformation around the basin is mostly displayed by fractures. Yet, folds and fault branches are observed near the tips of the boundary faults and near kink points of fault segments. Stress analysis obtained by the three-dimensional model is in general agreement with the orientation of fractures and location of high deformation regions in and around the basin. Based on our observations, we present a conceptual model which demonstrates the development of asymmetric basins in releasing bends and sheds light on the structures of similar large pull-apart basins.

Keywords Faults · Pull-apart basin · Strike–slip · Three dimensions · Numerical model · Ground-based LiDAR

✉ Amir Sagy
asagy@gsi.gov.il

[1] Geological Survey of Israel, 30 Malchei Israel St., Jerusalem, Israel

Introduction

Pull-apart basins are extensional structures developed in overlapping zones of segmented strike–slip faults. These basins are characterized by depressed regions bordered by two strike–slip segments and occasionally contain transverse faults that generate a typical rhomb shape in map view (Quennell 1959; Burchfield and Stewart 1966). Yet, many basins in releasing step zones deviate from this relatively simplified geometric description (Mann 2007). Moreover, while pull-apart is one of the most explored features in strike–slip fault regimes and its structure has been documented in many tectonic environments (e.g., Woodcock and Fischer 1986; Cunningham and Mann 2007), the real three-dimensional (3D) structure and the transformation of lateral displacement from one strike–slip segment to another are less familiar, as they are associated with subsurface fault architecture which is rarely exposed. Most of the information on the 3D structures of natural pull-apart basins is based on seismic surveys, seismologic observations and potential field methods that were collected in mature lithospheric-scale structures (e.g., ten Brink et al. 1993; Serpa et al. 1988; Armijo et al. 2002). However, these basins are usually highly deformed and their internal structures obscured by a thick sedimentary sequence (e.g., Garfunkel 1997). Some pull-apart basins are interpreted as generated deep rhomb-shaped structures in the brittle crust (e.g., ten Brink et al. 1993), whereas in others the two longitudinal faults converge at some depth, producing flower structures or a more complicated duplex geometry (Sylvester and Smith 1976; Aydin and Nur 1985; Woodcock and Fischer 1986).

One prominent approach to studying fault interaction in general and pull-apart basins in particular is based on

analogue laboratory experiments (Reches 1987; McClay and Dooley 1995; Dooley and McClay 1997; Basile and Brun 1999; Sims et al. 1999) or modeling (Rodgers 1980; Segall and Pollard 1980; Gölke et al. 1994; Katzman et al. 1995; Petrunin and Sobolev 2008; Ben-Avraham et al. 2010; Joshi and Hayashi 2010). These experiments enable investigating the evolution of the basin and the associated fault interactions under both different initial and boundary conditions. In some cases, these experiments appropriately reconstruct fault patterns which are comparable in map view to observations from natural examples. Yet, because the deep structure of natural basins is less known, it is hard to test the quality and the relevancy of such models along the vertical direction.

A complementary alternative is studying smaller natural basins as proxies for larger mature basins (e.g., Eyal et al. 1986; Bartov and Sagy 2004). The present analysis is focused on a mesoscale basin developed along an overlapping zone of parallel strike–slip segments (Fig. 1). Unique exposures of fault scarps and associated deformation zones in the basin area reveal major parts of the structure. The geometry of the fault surfaces is measured in high resolution using ground-based laser scanner (LiDAR) and is used to present a 3D picture of the structure. In addition, we analyze the fault kinematics and the deformation in the basin and in the nearby area. We demonstrate that the basin displays asymmetry in all three dimensions. The stress and strain fields associated with the present geometry are then calculated using a numerical 3D slip model. Finally, we present an alternative model for the evolution of the basin and suggest that such an evolution might control deviation from symmetric rhomb-shaped graben in other similar and larger basins.

Geological background

The Dalton pull-apart basin and the nearby outcrops are exposed in Upper Cretaceous limestone and chalk sediments in the Upper Galilee heights, northern Israel (Fig. 1). During the Cretaceous, the area was a part of a wide sedimentary platform and accumulated hundreds of meters of mostly carbonate sediments. Compressional structures developed in the area during the end of the Cretaceous to mid-Cenozoic times as evident from folds, local thickness variations of sedimentary formations and unconformities (Flexer et al. 1970; Garfunkel 1998). Uplift occurred from the end of the Eocene, and the area was exposed to erosional processes (Picard 1965). Since the Miocene, the region was mostly influenced by activity along the Dead Sea fault (Heimann and Ron 1993), which separates the Sinai subplate from the Arabian plate (Fig. 1a) and accumulates a left-lateral offset of more than 100 km (Quennell 1959; Bartov et al. 1980). The Galilee area (Fig. 1b) has since been subjected to several uplifts and arching episodes (Matmon et al. 1999).

Two sets of dense left-lateral and right-lateral strike–slip faults were identified in the Upper Galilee and southern Lebanon, oriented SE–NW and SW–NE, respectively (Freund 1970; Freund and Tarling 1979; Ron et al. 1984). These faults, usually <25 km long, displayed segmented and branched patterns. Measurements along these faults indicated vertical surfaces, horizontal striations and small pull-apart basins. The activity of the fault sets was dated to Late Miocene–early Pliocene times (Ron 1984; Ron and Eyal 1985). The two sets were interpreted as simultaneously activated, generating rotation of blocks in the region (Freund 1970). Paleomagnetic measurements confirmed that zones of NNW trending left-lateral faults rotated clockwise and zones of right-lateral faults rotated anticlockwise. These observations suggest regional shearing as well as N–S extension and E–W shortening of the Galilee heights, concurrently with the main activity along the Dead Sea fault (Freund 1970; Ron et al. 1984). The strike–slip deformation phase diminished in the Middle Pliocene and was followed by normal faulting on E–W-oriented faults (Ron and Eyal 1985; Matmon et al. 2003).

Field observations

General structure and rock units

The pull-apart basin, located on a hill 780 m high near the village of Dalton, is exposed on a ~250-m-long overlapping zone of a segmented ENE–WSW-oriented fault (Fig. 1c). The two right-stepping segments of this fault are marked here as the Western Main Fault and the Eastern Main Fault (WMF and EMF, respectively; see Fig. 2). The fault, with an overall exposed length of ~1.5 km, is related to the regional right-lateral strike–slip faults (Ron et al. 1984).

The rock layers around the pull-apart area dip moderately (~10°) southward with local variations. Three rock units are exposed (Fig. 2) and were identified and defined here by correlation to a nearby outcrop (Flexer 1964): A—layered gray limestone from the uppermost Turonian; B—limestone (usually called Ka'akule) from the base of the Senonian up to 50 m thick; and C—a thick Senonian chalk unit bedded above unit B.

Unit B is less rigid than unit A and can be identified by a brighter color and by its fractured appearance in outcrops. The unit is exposed on the basin margins and on the walls of the boundary faults. The overall thickness of the Senonian chalk in this area can reach 200 m, yet based on correlation to a nearby studied outcrop (Flexer 1964), unit C, which is exposed in the basin, contains only the two bottom

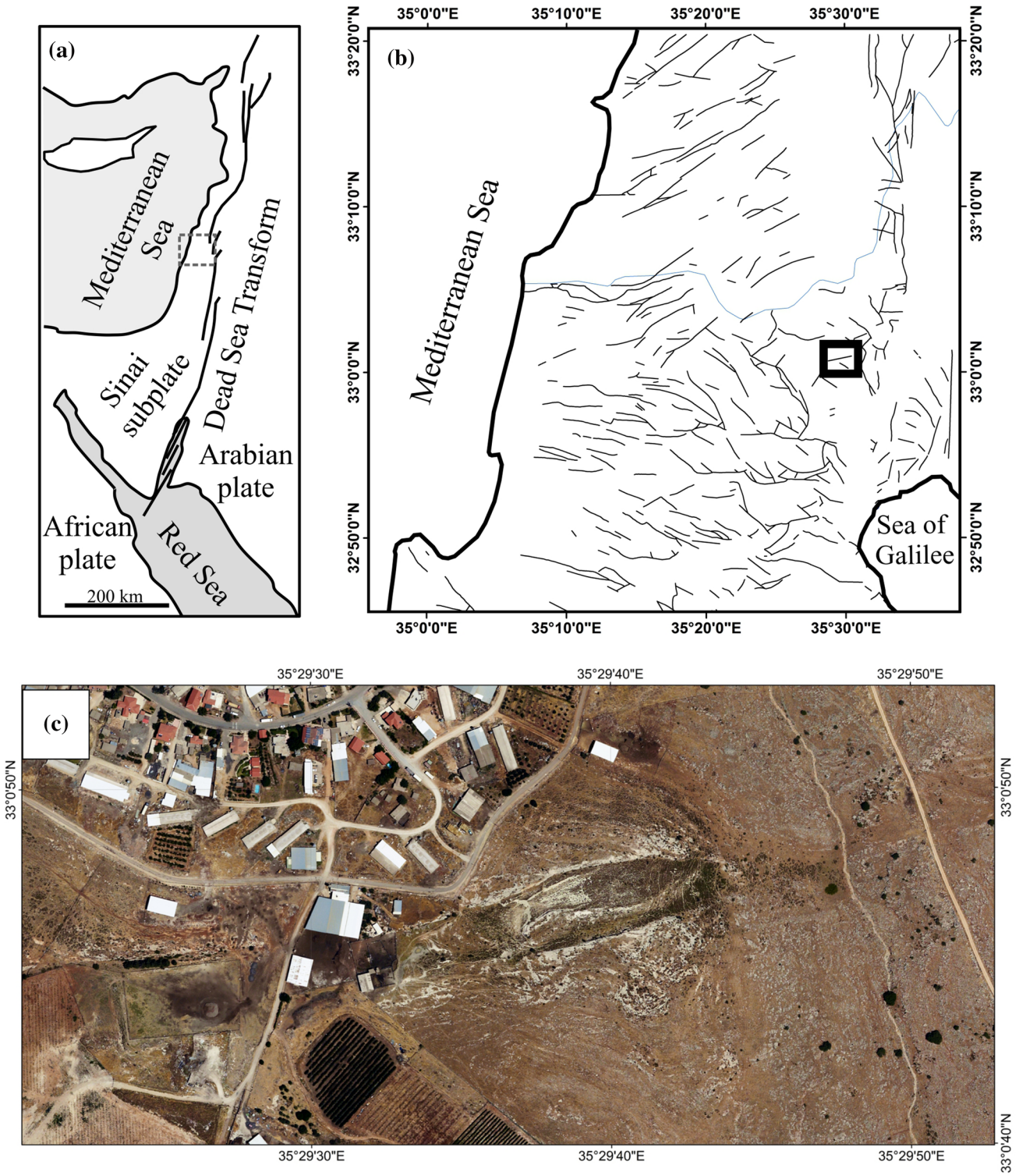

Fig. 1 Dalton pull-apart basin. **a** Regional tectonic configuration. **b** Fault traces in the Galilee heights and south Lebanon (modified from Sneh et al. 1998). **c** Aerial photograph of the pull-apart basin and the segmented fault near Dalton village. *Squares* in **a** and **b** mark the locations of **b** and **c**, respectively

members of the Senonian chalk. Consequently, we evaluate the maximal stratigraphic separation between the basin and its margins to be <50 m. Based on direct field measurements of the exposed rock units, the minimal stratigraphic

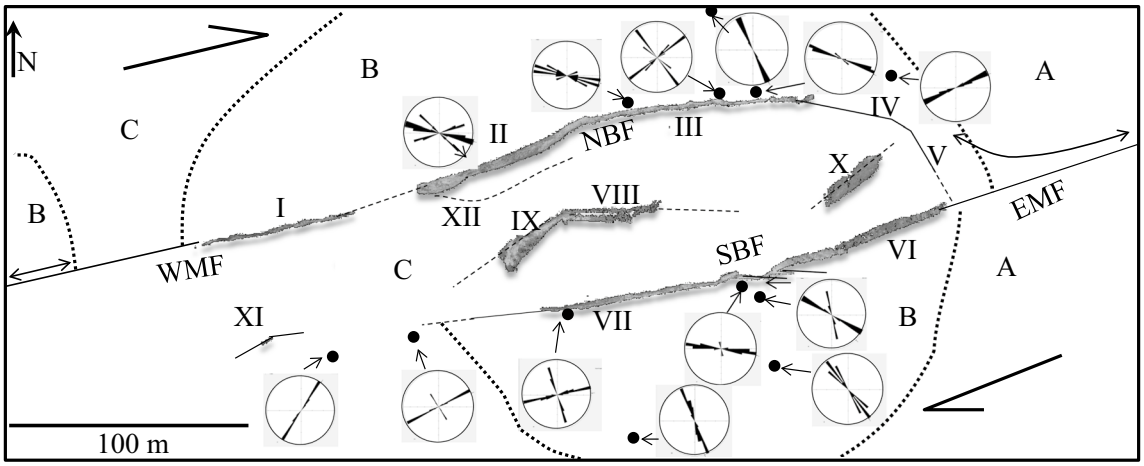

Fig. 2 Map view showing location of rock units, fault traces, fractures and folds near the Dalton pull-apart basin. Different rock units are marked by *A*, *B* and *C* and bordered by *dotted lines*; *roman letters* mark different fault segments. *Thick lines* are traces of faults, appear as scarps and mapped by ground-based LiDAR. *Continuous lines* mark fault traces clearly identified and *dashed lines* mark evaluated fault traces (see text). Rose diagrams point to fracture orientations in a given location (marked by *black dots*). WMF and EMF are the Western and Eastern Main Faults, respectively. NBF and SBF are the Northern and Southern Boundary Faults, respectively. *Arrows* marks the right-lateral slip along the structure

separation in the northwestern part of the structure was found to be more than 10 m.

The internal structure of the pull-apart basin is much more eroded than its margins due to the difference between the mechanical properties of the chalk and the limestone. Therefore, some of the faults around it are exposed by morphological scarps with striated slip surfaces along them while other faults can be recognized by linear separation between rock types. On the other hand, the faults inside the basin are morphologically less prominent.

Fault segments

Measurements of fault surfaces were taken using the Leica ScanStation 2 laser scanner that provides subcentimeter accuracy for the presented distances (up to 100 m). Point clouds that were generated using measurements from six different locations were integrated to create a complete picture of the exposed fault scarps and fault traces of the basin.

Local orientations of fault strike, dip, slip surfaces and slickensides along different segments were measured. The map presented in Fig. 2 displays three types of fault traces: faults scarps identified by slip surfaces that have a prominent morphological feature; faults identified by lithological separation; and faults whose existence is assumed based mostly on the appearance of topographical steps or cliffs. We show below that the northern and the southern boundary faults are structurally and geometrically different, generating an asymmetrical structure.

West of the overlapping zone, the WMF is exposed by about a 4 m high, steep and almost vertical cliff with smooth slip surfaces along it (Fig. 3). The average dip is 88°/167° while striations rake 4°–5° westward. The relief is visible to about 80 m, fading eastward and westward. East of the overlapping zone, the EMF has no morphological manifestation, but its traces can easily be followed as an almost abrupt linear separation between different sequences of layers and inclinations.

The pull-apart boundary faults generate an almost continuous pattern, which can be divided to several segments. The northern boundary fault (NBF) dips southward and includes three main segments (marked II, III and IV in Fig. 2). Segment II dips 65° and strikes 075°. The scarp reaches its maximal height of 7 m at the western part of the segment (Fig. 4a).

Measurements of striations in two locations along Segment II demonstrated rakes of 7° and 14° (Fig. 4b). In addition, short slip surfaces at steep angles from the main surface were documented with oblique striations, penetrating the rock wall to a few dozens of centimeters from the main surface but usually diminishing further away. The orientation of these slip surfaces and the orientation of striations along them resembling Riedel shear fractures developed, respectively, to the right-lateral slip along the main surface (Tchalenko 1970). The scarp becomes lower eastward.

Segment III appears as a small step at a height of about 0.5 m, which diminishes eastward. Further eastward, the surface strikes from 75° to 85° while striation orientations measured in two nearby locations were 5° and 16°. Segment IV generates a topographic slope (Fig. 5) that bends southward while its continuation in the eastern part of the structure, segment V, merges with the southern boundary fault (SBF) of the structure.

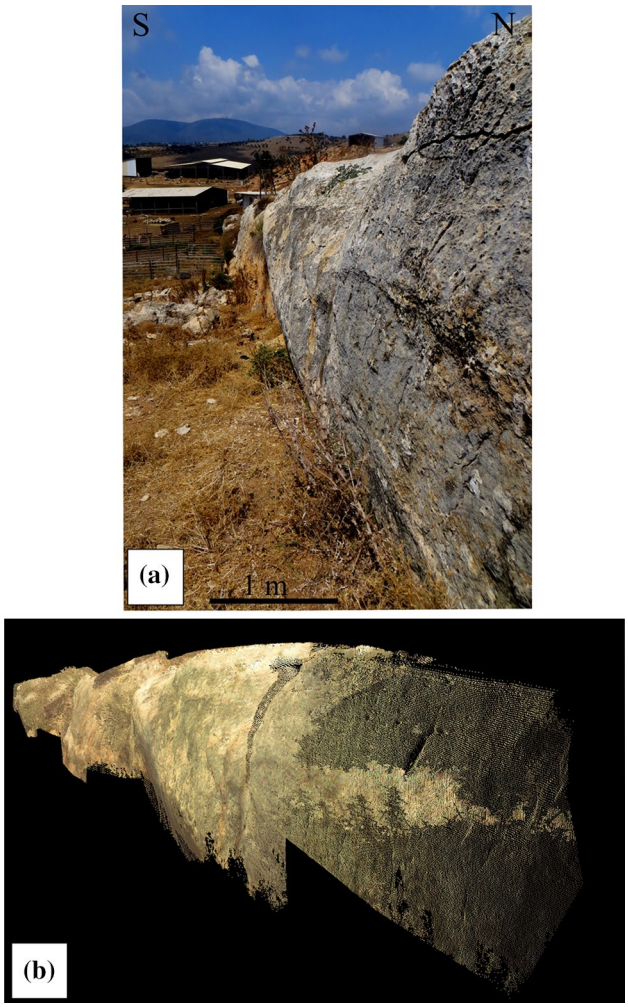

Fig. 3 A picture (**a**) and a LiDAR imaging (**b**) showing an oblique view of a striated surface on segment I of the WMF

The SBF is steeper and more planar than the NBF and is defined by two fault segments, VI and VII (Figs. 2, 5). Segment VII is a cliff with a maximum height of 2 m near its eastern tip and an average dip of 85°/352°. In some locations, the fault surface is essentially vertical and even inclined southward. Measurements of striations yielded a rake of 15° westward. Segment VI is identified by a scarp only in its connection to segment VII, while further to the east it is recognized by a topographic slope and by a sharp planar border between units B and C (Figs. 2, 3). The connecting area between the two segments (VII and VI) consists of three small fault segments-oriented E–W and arranged in left stepping en-echelon geometry (Fig. 2).

Four fault segments were interpreted in the interior part of the pull-apart structure. Three of them are arranged in a zigzag geometry (segments VIII, IX and X in Fig. 2). Fault VIII (Fig. 3) is the only one that displays a clear vertical slip surface which strikes 085°, while the other two (IX and X in Fig. 2) are steep morphological steps.

West of the overlapping zone a vertical slip surface striking 055° is observed creating a small step of <50 cm which is exposed for about 10 m (XI in Fig. 2). No other significant faults are observed near the pull-apart basin.

Structural reconstruction

Clear geometrical asymmetry between the NBF (segments I, III, IV) and the SBF (segments VI, VII) is distinguished. Figure 2 shows the NBF is a continuous segmented fault with variations in strike orientation. The easternmost segment of the NBF (segment V) merges almost orthogonally into the SBF and generates the eastern transverse border of the basin (Fig. 3). In addition, the NBF in the overlapping area dips toward the basin while its continuation westward, the WMF, is vertical. The surface of the SBF, on the other hand, is almost vertical along the entire overlapping zone. The stratigraphic relationship between rock units and orientations of slickensides indicates oblique dextral displacement with maximal rakes of about 15° in both boundary faults. The western border of the basin is not well defined, and there is no indication of a transverse or diagonal fault bordering it.

The continuity and the quality of the field observations enable reliable reconstruction of the 3D structure. Patches of fault surfaces were separated from other topographical features in the laser scanner measurements and later used to generate best-fit fault plains. The extrapolations of the planes enabled full 3D structure geometry. Assuming the same architecture continues to depth, the two longitudinal faults emerge near the western tip of the SBF at a depth of about the 300 m, generating an asymmetric V-shaped structure in vertical cross section. Based on the regional stratigraphy and the geological history during the deformation time, the maximum sedimentary cover above the present outcrop was probably less than a few hundred meters thick. This observation suggests that the vertical dimension of the basin from the merging line to the surface was probably on a scale of a few hundred meters.

Folds and fractures

Folds and fractures were measured and serve as indicators for local stress and strain orientations. Joint sets were used as indicators for the orientation of the least compressional local stress while conjugate shear fractures were used as indicators for the maximal local compression (Jaeger et al. 2009). Fractures in 12 locations around the overlapping zone were measured and analyzed based on the relatively well-exposed fracture sets in unit B (Fig. 2). The chalk in the interior structure (unit C) was highly fragmented, and

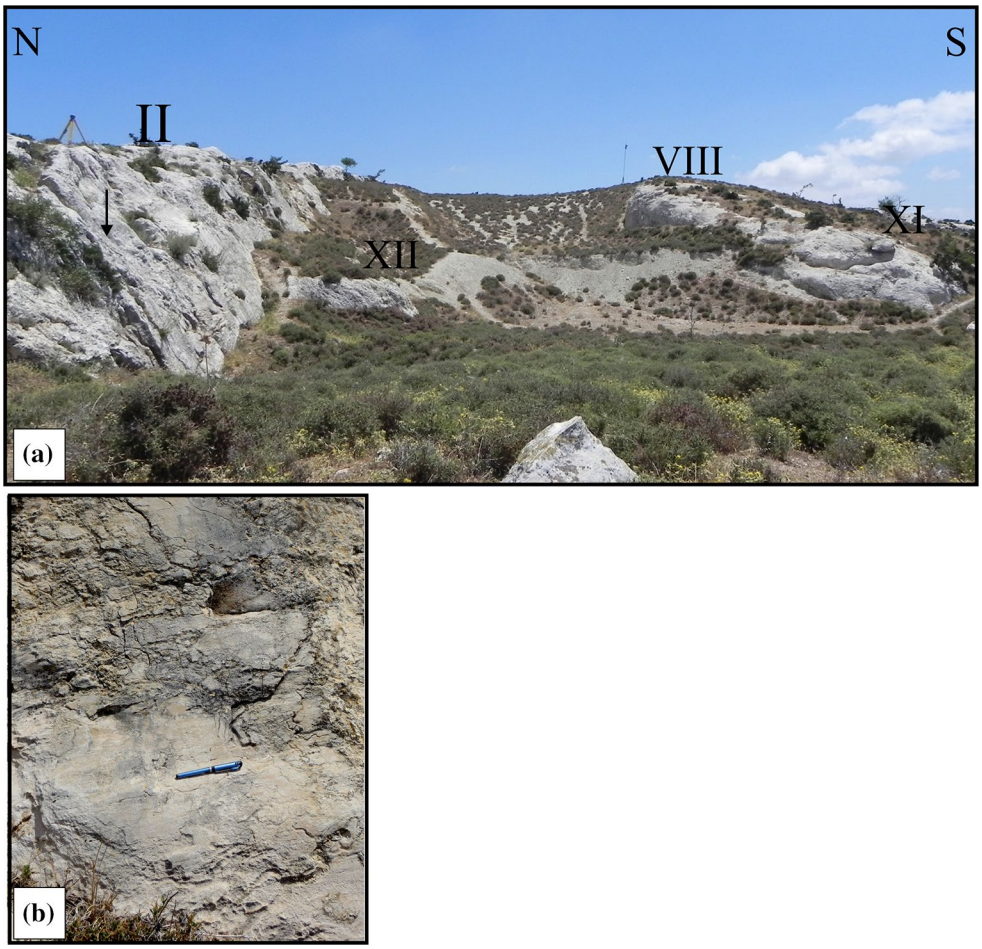

Fig. 4 Fault scarps in the northwestern part of the Dalton basin show segment II of the NBF and the internal segments VIII and XI (**a**). The *black arrow* points to the location of the abrasive oblique striation shown in (**b**)

no clear dominant fracture sets could be identified. Rocks of unit A are generally not fractured. In a given outcrop, we measured orientations of fractures that were continuous for at least one meter on the top surface of the layers (map view). In most of the stations, fractures around the structure were identified as joints (tensile fractures) with no indication of shear along them. Yet, some fractures which displayed striations with normal or oblique components were identified as small faults. For example, in a single location, near segment II, three sets of fractures were identified and interpreted as a conjugate fault set and a joint set. Nearby, a shear fracture oriented subparallel to segment II is observed along a few meters. A few joints branch off of it, generating typical horsetail and splay joints (Fig. 6). The hierarchy which consists of splay joints associated with strike–slip faults was already documented in the field (Segall and Pollard 1983), and it is assumed, based on experimental observations, that they curve parallel to the maximum local compressive stress (e.g., Brace and Bombolakis 1963).

Two folds were mapped east and west of the overlapping zone (Fig. 2). Both folds appear as monoclinic flexures associated with the WMF and the EMF. The eastern monocline can be recognized in unit A by tilted blocks east of the structure (Fig. 2), with layer inclinations increasing southward, from 10°/170° to 40°/178° alongside the EMF (Fig. 5). Near the basin, the dip orientation changes to SSW, as indicated by the bend of the fold axis in its western tip (Fig. 2). A fold with a smaller wavelength and more moderate inclinations was observed in rocks from unit B near the WMF, west of the overlapping zone, with dips varying from 8°/200° about 50 m from the fault to 25°/190° right next to the fault surface. In contrast to the eastern folding area, the location of the western fold is further away, about 150 m from the overlapping zone.

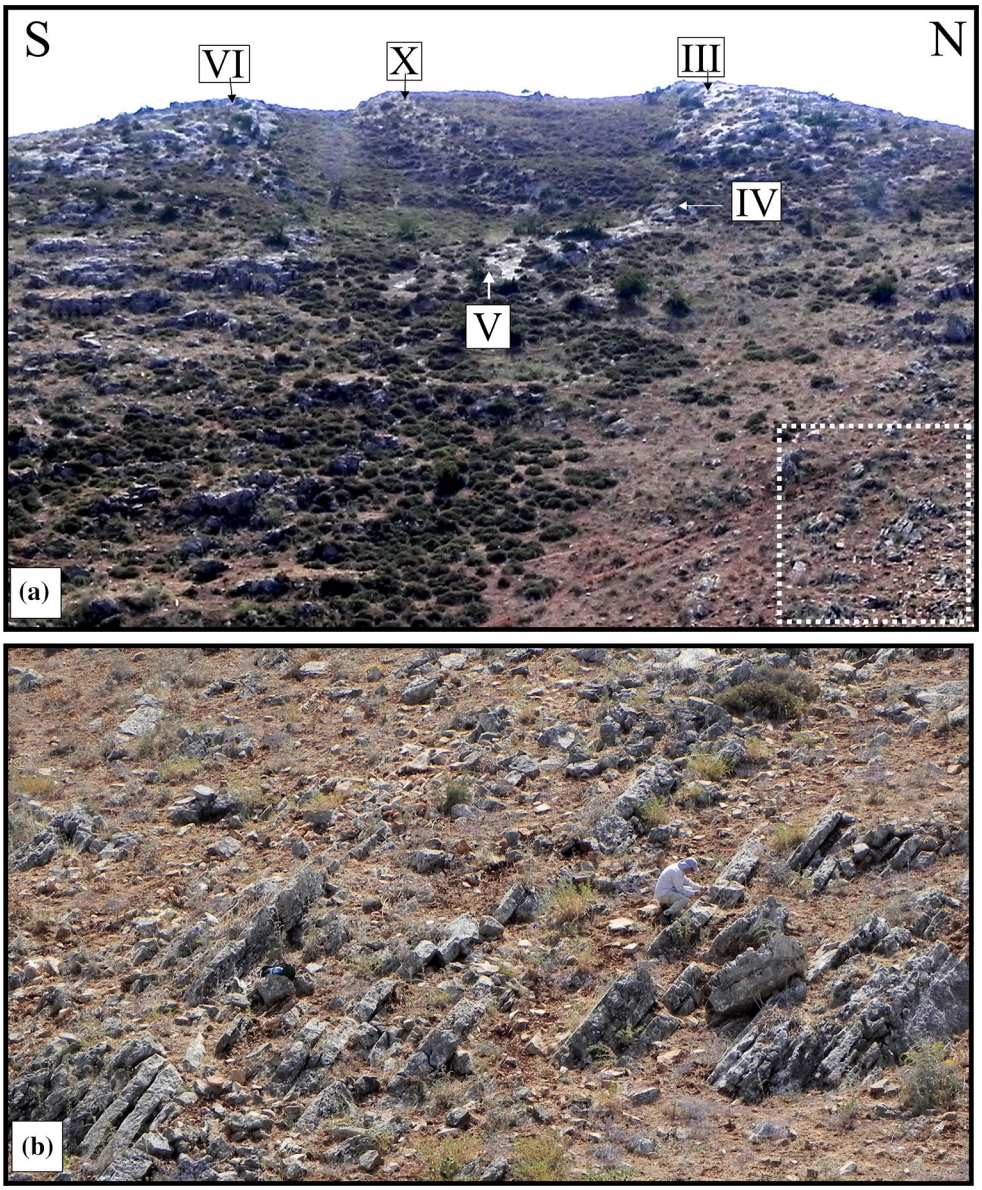

Fig. 5 Eastern region of the Dalton pull-apart basin. **a** The transverse fault segment *V* connects the NBF (segments III, IV) to the SBF (segment VI). **b** Tilted layers in the folded area east of the pull-apart basin (see Fig. 2). The location of **b** is marked by a *square* in **a**

Modeling the deformation near an asymmetric pull-apart basin

Model setup and results

A 3D elastic dislocation model (e.g., Massonnet et al. 1993; Savage and Lisowski 1995) is applied in order to simulate the deformational pattern in and around the Dalton pull-apart basin. The aim of this simple model is to calculate the stress variations resulting from a relatively small lateral slip (1 m in the present example) along such an asymmetrical V-shaped basin and to compare it with the field observations. The solutions for surface deformation due to rectangular dislocations in homogeneous elastic half-space media were given by Okada (1985, 1992). Each rectangular dislocation plane represents a single fault segment and is defined by seven parameters: slip; coordinates; length; depth; strike; dip; and rake angles. We assumed a uniform slip along each segment plane and typical elastic moduli for the upper continental crust: shear modulus, $\mu = 30$ GPa; and Poisson ratio, $\nu = 0.25$. We constrained the fault geometry and slip parameters based on our detailed field observations. The LiDAR measurements (Fig. 7) were used to constrain the location and segmentation of the fault planes

Fig. 6 Splay joints (marked by *orange arrows*) branched off from a shear fracture (marked by the *red arrow*) that itself branches in an acute angle off the NBF, near segment II

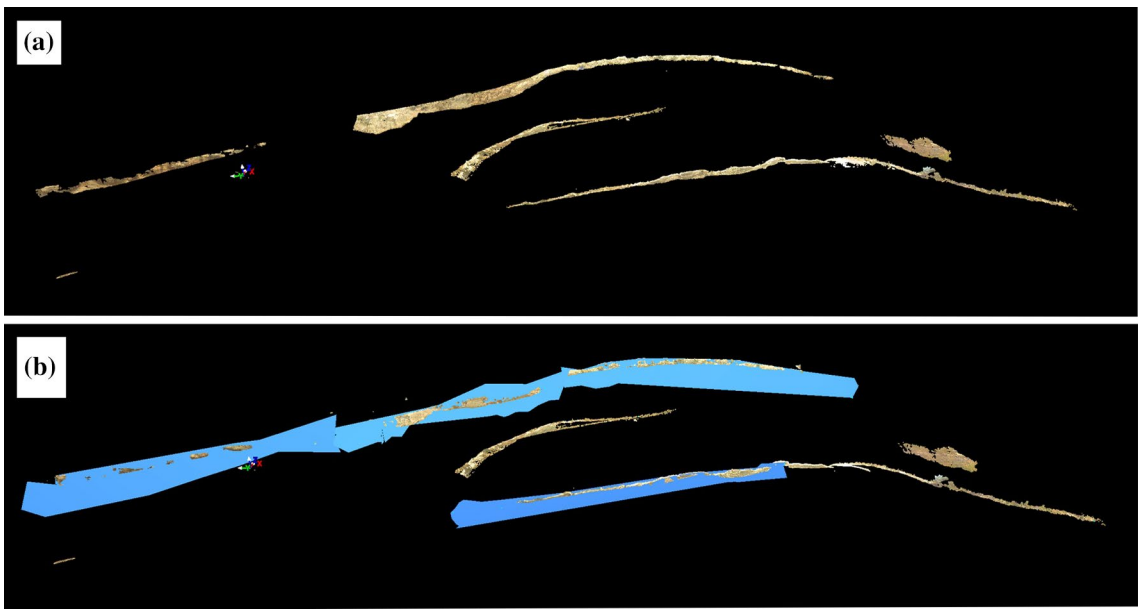

Fig. 7 LiDAR mapping of the exposed fault segments and fault scarps in the Dalton pull-apart basin. Scannings were performed from five different locations and integrated to generate a complete picture of the exposed part of the structure. **a** All LiDAR data which are not related to faults are cleaned, leaving only fault surfaces. **b** Best-fit planes were calculated for the fault segments based solely on striated regions

and segment lengths, as well as the overall dip and strike angles of each segment.

The location and dip of fault segments were used to identify the depth of each segment along the pull-apart structure. The Dalton pull-apart basin was divided into six boundary dislocations. For simplicity reasons, segments IV and V in Fig. 2 were simulated as a single dislocation while internal segments IX, VIII and X and external fault segment XI were not modeled. The easternmost and westernmost dislocations (segments WMF and EMF in Fig. 2) were simulated as long and deep (5 km) dislocations. The depths of other dislocations were between 150 and 300 m according to the dip and distance of each dislocation from other fault segments. The rake angles for any given dislocation were defined by the field measurements of the orientation of striations.

The final fault trace of the modeled dislocations geometry is presented in Fig. 8. The calculations presented here were made assuming 1 m of slip along the strike direction of the WMF and the EMF. Then, the slip vector on each

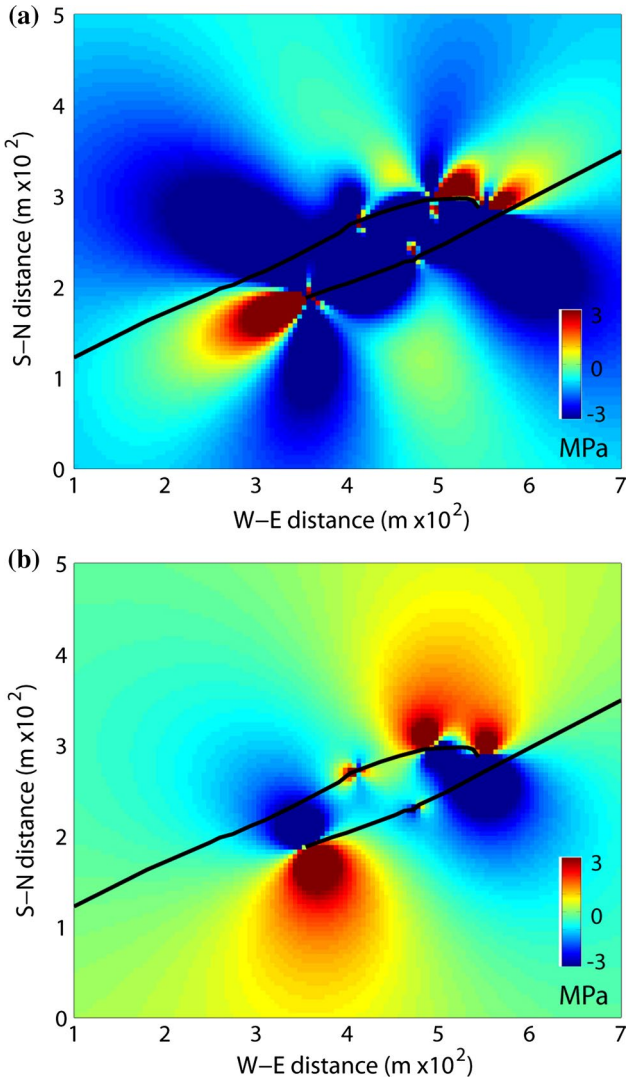

Fig. 8 Shear stress (**a**) and mean stress (**b**) calculated for an asymmetric basin using a dislocation slip model (see text for more details). *Thick black lines* mark faults traces

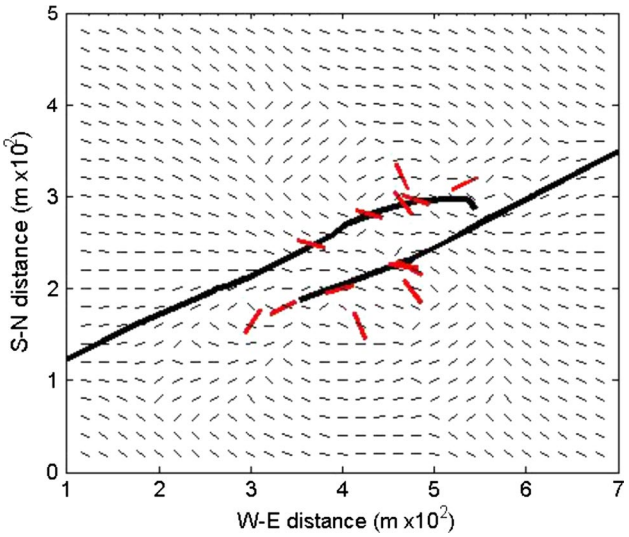

Fig. 9 Observed (*red lines*) and modeled (*thin black lines*) tensile crack orientations. The orientation of the *black lines* is calculated as the normal direction to the least principle stress

segment was calculated according to the dip, strike and rake angles on each segment. Direct results of the simulations are the strain and stress fields.

We calculated the principal stress (σ_i) and strain (ε_i) fields due to our pull-apart slip model. The principal stress field obtained reveals high stress variations in and around the pull-apart basin (Fig. 8). Figure 8a shows the calculated shear stress variations. High shear stress (and Coulomb stress; not shown here) values were found near the edges of the structure and in some places within the pull-apart basin. These locations within the basin are in general agreement with the locations of fault segments within the pull-apart basin (segments IX–X in Fig. 2). As expected for a right-lateral strike–slip structure, high stress values were found near the eastern tip of the structure (Fig. 8b). This region is also the area in which tilted blocks and an increase in rock layer inclination were observed. Based on the results of the principal stress field, we calculated the directions of the preferred orientations for crack opening, assuming that this direction is perpendicular to the minimum principal stress, $\sigma 3$. Figure 9 shows a pattern of short lines which are perpendicular to the local $\sigma 3$. Figure 9 also shows a comparison between the calculated and the observed crack orientations. As shown in the figure, general agreement between measured and calculated stress orientation is found just next to the structure boundary faults. These observations together with the locations of regions with high stress variations suggest that our simplified model explains the deformational features near the basin. Some discrepancy between the observations and model predictions near the fault tip and away for the structure (>30 m) is discussed in the next section.

Model predictions and implications

Our model presents the deformational pattern associated with the development of an asymmetrical V-shaped pull-apart basin. In this sense, this model is different from previous 3D models which mostly focused on the evolution of basins generated by interaction of parallel strike–slip segments (Katzman et al. 1995; Petrunin and Sobolev 2008; Ye et al. 2015).

The predicted high stress levels occur near the eastern and the western margins of the basin, close to locations of the observed main deformational features. Fault segment XI (Fig. 2) west of the pull-apart basin is found in an area of high shear stresses, while the folded area near the eastern

tip of the basin (Figs. 2, 5) is in an area of high mean stress levels (Fig. 8). According to the model, fracture and small faults are more prominent in kink points of segments, for example, near the area connected between segments VI and VII (Figs. 2, 8).

Our model predicts abrupt stress variations close to the faults of the basin (Fig. 8). This stress pattern can explain the local variations observed in fracture orientations around the basin (Fig. 2). The orientations of most joints observed close to the fault segments are in agreement with model predictions. Some discrepancy exists between the model predictions and the observations obtained near the eastern-most edge of the structure and at locations away from the faults (>30 m; Fig. 9). We note that the model predicts the stress state under the present geometry but it is likely that some of the measured fractures and folds developed during previous stages of the structure's evolution, under different local stress orientations. Later deformation episodes might also affect the observations; for example, the model failed to predict the NNW–SSE orientations measured in the southern and the northern stations (Fig. 2). These might have been generated later, under a different regional stress field (see Eyal and Reches 1983).

Further discrepancy between the elastic predictions and the actual deformation naturally increases with the continuation of the deformation and the development of irreversible deformation (e.g., Hamiel et al. 2004). The fact that near one tip of the basin the deformation is manifested by folding while near the other it is brittle might be related to the lithological differences between the two regions (Fig. 2) and to the asymmetry in fault geometry.

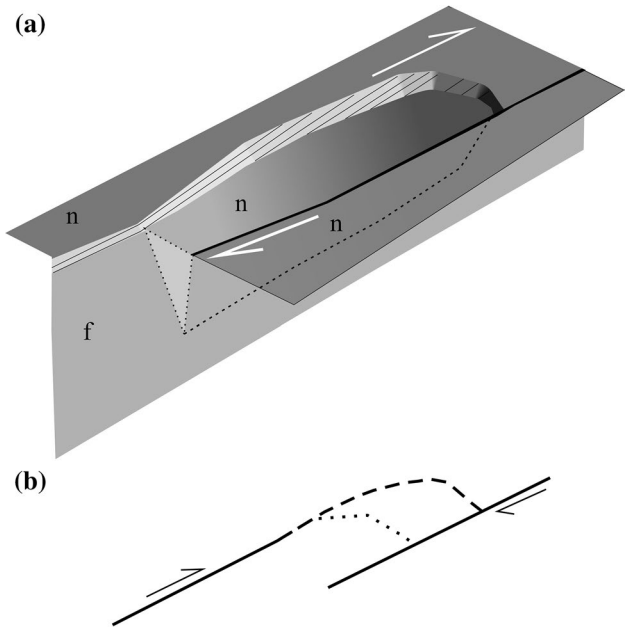

Fig. 10 A simple conceptual model of the Dalton pull-apart basin. **a** Three-dimensional scheme showing horizontal surface (marked by "*n*"), which is faulted by right-lateral displacement along the strike–slip fault segments. *Dotted lines* mark lines branching off the main fault. **b** Two stages in the basin evolution are interpreted in two-dimensional scheme (map view). Original interaction of the subparallel fault traces is marked by the *dotted line*; later extension is marked by the *dashed line*

Discussion

The Dalton basin presents some unique geometrical aspects that deviate from the basic and relatively simple rhomb-shaped pull-apart model. In the basic model, a transverse planar fault is generated between the edges of the subparallel strike–slip fault segments and the lateral extension is defined by the size of the symmetric rhomb-shaped basin. The length of the basin is therefore similar to the overall lateral displacement along it (e.g., Quennell 1959; Garfunkel 1997); consequently, a transverse fault is usually placed in many analogue models as an initial geometric condition. Here, we suggest that the asymmetrical geometry of the Dalton basin represents a different fault interaction and basin evolution. Since direct indications for the amount of horizontal slip along the faults are absent, the stratigraphic separation and the orientation of striations (rake) in the overlapping zone can be used for evaluating the overall lateral displacement. Assuming a rake of 15° westward along the northern and southern boundary faults and a stratigraphic separation of 10–50 m, we can evaluate the overall horizontal displacement as a value between 40 and 180 m. Although this is a rough calculation, it constrains the overall displacement along the faults, which is shorter than the length of the overlapping zone (~250 m). We therefore conclude that the length of the overlapping area is larger than the total lateral displacement. This result implies that the length of the structure is no longer an indication of the overall slip in asymmetrical pull-apart basins.

The Dalton basin displays asymmetry in all three dimensions. Figure 10 presents a diagram simplifying the general 3D architecture of the faults bordering the pull-apart basin. The longitudinal asymmetry of the basin is reflected by the appearance of a single bordering transverse fault (segment V in Fig. 2). The western border of the overlapping zone is displayed by the diminishing of the SBF scarp and by a transition from a vertical fault (segment I) to an inclined fault (segment II) in the north. The lateral asymmetry is also displayed by the segmented NBF relative to the SBF (Fig. 2), while the vertical asymmetry is displayed by the southward dipping of the NBF and the generation of an asymmetric V-shaped basin. The patterns of the bordering faults in map view (Figs. 1, 2) reflect an elongated and less rhombic structure.

The observations above summarized the structural deviations of the basin from the basic pull-apart model. A slightly different interpretation for the basin evolution is therefore presented in Fig. 10. According to this scenario, the interaction of the two subparallel faults is not expressed by a transverse planar fault that connects the edges of the subparallel segments, but rather by evolution of inclined branch that is bent in the surface and that joins the other strike–slip segment at depth (Fig. 10a). Therefore, a more elongated and asymmetrical basin is predicted to evolve, with less correlation between the lateral displacement and the basin length. Continuation of the lateral displacement is absorbed by strike–slip along the longitudinal faults (NBF and SBF) and by normal faulting along the transverse fault (Fig. 10b). Such an extension is probably associated with internal deformation of the basin, which is not interpreted here.

The scenario presented is slightly different from a simple pull-apart model, and it explains the main observations. We note that the observations and this conceptual model cannot discriminate between branching (lensing) of a single propagating strike–slip fault and joining of two individual subparallel segments.

Finally, the interpreted basin geometry and evolution might be relevant for understanding the structural features in other basins along strike–slip faults. Asymmetry between bordering faults has been documented in several mature basins (Ben-Avraham 1992; Brew et al. 2001; Hinsch et al. 2005; Wetzler et al. 2015). For example, the Dead Sea pull-apart basin displays elongated patterns, a steep eastern bordering fault and less coherent western margins (e.g., Garfunkel 1997). The asymmetric V-shaped cross section of the Dalton structure is typical in some other large and small basins. For example, an asymmetrical V-shaped structure was suggested, based on seismic interpretation, for the Vienna basin (Hinsch et al. 2005).

On extremely different scales, laboratory experiments indicated that such geometry can be developed when a subsurface strike–slip fault propagates to near surface regions (Tchalenko 1970; Naylor et al. 1986). Therefore, the Dalton Basin might be interpreted as a large Riedel shear structure. We note that such a V-shaped structure is different form a rhomb-shaped graben with very steep boundary faults that is crossed by younger faults developed during latter phase of the structure evolution (e.g., Schattner and Weinberger 2008).

Summary and conclusions

The exposure of faults near the Dalton basin enabled us to reconstruct the geometry of this basin and to present a realistic model of the structure and the nearby region. We find that the geometry of the basin is asymmetric in all three dimensions and deviates from the typical rhomb-shaped structure. The basin, whose patterns in map view are elongated, is not bordered by transverse or diagonal faults on its western edge. In vertical transverse cross section, the basin displays an asymmetrical branching structure. The amount of lateral displacement along the basin is smaller than the length of the overlapping zone and is localized on oblique bordering strike–slip faults.

The deformation around the basin is moderate, except near the tips of the bordering faults. Fracture orientations vary locally near the basin's bordering faults, and a flexure is observed near the eastern edge of the basin. 3D modeling of stress variations demonstrates high stress values near the eastern and the western borders of the structure.

We present an alternative conceptual model for the development of an elongated pull-apart basin. This model suggests that a non-planar fault branch transfers the motion between the two subparallel strike–slip segments (Fig. 10). This distinctive fault interaction can explain both the 3D asymmetry of the basin geometry as well as the limited correlation between basin length and lateral displacement. We suggest that original non-planar fault interactions can strongly affect the continuation of basin evolution and can be the key to the evolution of asymmetrical and less rhombic basins in releasing bends along strike–slip faults.

Acknowledgments This work is dedicated to the memory of Prof. Hagai Ron who first showed us the Dalton basin during a field trip. We thank Yaakov Mizrachi for his help in the fieldwork and Michele Cooke for helpful discussion. We thank the editor Wolf-Christian Dullo and the reviewers Dickson Cunningham and Ariel Heimann for their insightful comments and constructive review which helped improve this manuscript.

References

Armijo R, Meyer B, Navarro S, King G, Barka A (2002) Asymmetric slip partitioning in the Sea of Marmara pull-apart: a clue to propagation processes of the North Anatolian Fault? Terra Nova 14:80–86

Aydin A, Nur A (1985) The types and roles of stepovers in strike slip tectonics. In: Biddle KT, Christie-Blick N (eds) Strike-slip deformation, basin formation, and sedimentation. Society of economic paleontologists and mineralogists, special publication, vol 37, pp 35–45

Bartov Y, Sagy A (2004) Late Pleistocene extension and strike-slip in the Dead Sea basin. Geol Mag 141:565–572

Bartov Y, Steinitz G, Eyal M, Eyal Y (1980) Sinistral movement along the Gulf of Aqaba—its age and relation to the opening of the Red Sea. Nature 285:220–221

Basile C, Brun JP (1999) Transtensional faulting patterns ranging from pull-apart basins to transform continental margins: an experimental investigation. J Struct Geol 21:23–37

Ben-Avraham Z (1992) Development of asymmetric basins along continental transform faults. Tectonophysics 215(1):209–220

Ben-Avraham Z, Lyakhovsky V, Schubert G (2010) Drop-down formation of deep basins along the Dead Sea and other strike-slip fault systems. Geophys J Int 181:185–197

Brace WFD, Bombolakis EG (1963) A note on brittle crack growth in compression. J Geophys Res 68:3709–3713
Brew G, Lupa J, Barazangi M, Sawaf T, Al-Iman A, Zaza T (2001) Structure and tectonic development of the Ghab basin and the Dead Sea fault system, Syria. J Geol Soc 158(4):665–674
Burchfield BC, Stewart JH (1966) "Pull-apart" origin of the central segment of Death Valley, California. Geol Soc Am Bull 77:439–442
Cunningham WD, Mann P (2007) Tectonics of strike-slip restraining and releasing bends. Geol Soc Lond Spec Publ 290:1–12
Dooley T, McClay K (1997) Analog modeling of pull-apart basins. AAPG Bull 81:1804–1826
Eyal Y, Reches Z (1983) Tectonic analysis of the Dead Sea Rift Region since the Late-Cretaceous based on mesostructures. Tectonics 2:167–185
Eyal Y, Eyal M, Bartov Y, Steinitz G, Folkman Y (1986) The origin of the Bir Zreir rhomb-shaped graben, eastern Sinai. Tectonics 5:267–277
Flexer A (1964) On the paleogeography of the Senonian and the Maastrichtian in northern Israel. PhD thesis, Hebrew University of Jerusalem **(in Hebrew)**
Flexer A, Freund R, Reiss Z, Buchbinder B (1970) Santonian paleostructure of the Galilee. Isr J Earth Sci 19:141–146
Freund R (1970) The geometry of faulting in Galilee. Isr J Earth Sci 19:117–140
Freund R, Tarling DH (1979) Preliminary Mesozoic palaeomagnetic results from Israel and inferences for a microplate structure in the Lebanon. Tectonophysics 60:189–205
Garfunkel Z (1997) The history and formation of the Dead Sea basin. In: Niemi T, BenAvraham Z, Gat J (eds) The Dead Sea: the lake and its setting. Oxford University Press, New York, pp 36–56
Garfunkel Z (1998) Constraints on the origin and history of the Eastern Mediterranean basin. Tectonophysics 298:5–35
Gölke M, Cloetingh S, Fuchs K (1994) Finite-element modelling of pull-apart basin formation. Tectonophysics 240:45–57
Hamiel Y, Lyakhovsky V, Agnon A (2004) Coupled evolution of damage and porosity in poroelastic media: theory and applications to deformation of porous rocks. Geophys J Int 156:701–713
Heimann A, Ron H (1993) Geometric changes of plate boundaries along part of the northern Dead Sea transform: geochronologic and paleomagnetic evidence. Tectonics 12:477–491
Hinsch R, Decker K, Wagreich M (2005) 3-D mapping of segmented active faults in the southern Vienna Basin. Quat Sci Rev 24:321–336
Jaeger JC, Cook NG, Zimmerman R (2009) Fundamentals of rock mechanics, 4th edn. Wiley, New York
Joshi GR, Hayashi D (2010) Finite element modelling of the pull-apart formation: implication for tectonics of Bengo Co pull-apart basin, southern Tibet. Nat Sci 2:654
Katzman R, ten Brink US, Lin J (1995) Three-dimensional modeling of pull-apart basins: implications for the tectonics of the Dead Sea basin. J Geophys Res Solid Earth 100:6295–6312
Mann P (2007) Global catalogue, classification and tectonic origins of restraining-and releasing bends on active and ancient strike-slip fault systems. Geol Soc Lond Spec Publ 290(1):13–142
Massonnet D, Rossi M, Carmona CS, Adragna FDR, Peltzer G, Feigl K, Rabaute T (1993) The displacement field of the Landers earthquake mapped by radar interferometry. Nature 364:138–142
Matmon A, Enzel Y, Zilberman E, Heimann A (1999) Late Pliocene and Pleistocene reversal of drainage systems in northern Israel: tectonic implications. Geomorphology 28:43–59
Matmon A, Wdowinski S, Hall JK (2003) Morphological and structural relations in the Galilee extensional domain, northern Israel. Tectonophysics 371:223–241
McClay K, Dooley T (1995) Analogue models of pull-apart basins. Geology 23:711–714
Naylor MA, Mandl GT, Supesteijn CHK (1986) Fault geometries in basement-induced wrench faulting under different initial stress states. J Struct Geol 8:737–752
Okada Y (1985) Surface deformation due to shear and tensile faults in a half-space. Bull Seismol Soc Am 75:1135–1154
Okada Y (1992) Internal deformation due to shear and tensile faults in a half-space. Bull Seismol Soc Am 82:1018–1040
Petrunin AG, Sobolev SV (2008) Three-dimensional numerical models of the evolution of pull-apart basins. Phys Earth Planet Inter 171:387–399
Picard L (1965) The geological evolution of the quaternary in the central-northern Jordan graben, Israel. Geol Soc Am 84:337–366
Quennell A (1959) Tectonics of the Dead Sea rift. In: Proceedings of the 20th international geological congress, Mexico, pp 385–403
Reches Z (1987) Mechanical aspects of pull-apart basins and push-up swells with applications to the Dead Sea transform. Tectonophysics 141:75–88
Rodgers DA (1980) Analysis of pull-apart basin development produced by en echelon strike-slip faults. In: Balance PF, Reading HG (eds) Sedimentation in oblique-slip mobile zones. International Association of Sedimentologists Special Publication vol 4, pp 27–41
Ron H (1984) Paleomagnetic investigation of the fault structure of Galilee-northern Israel. PhD thesis, Hebrew University of Jerusalem
Ron H, Eyal Y (1985) Intraplate deformation by block rotation and mesostructures along the Dead Sea transform, northern Israel. Tectonics 4:85–105
Ron H, Freund R, Garfunkel Z, Nur A (1984) Block rotation by strike-slip faulting: structural and paleomagnetic evidence. J Geophys Res 89:6256–6270
Savage JC, Lisowski M (1995) Strain accumulation in Owens Valley, California, 1974 to 1988. Bull Seismol Soc Am 85:151–158
Schattner U, Weinberger R (2008) A mid-Pleistocene deformation transition in the Hula basin, northern Israel: Implications for the tectonic evolution of the Dead Sea Fault. Geochem Geophys Geosyst 9(7). doi:10.1029/2007GC001937
Segall P, Pollard DD (1980) Mechanics of discontinuous faults. J Geophys Res 85:4337–4350
Segall P, Pollard DD (1983) Nucleation and growth of strike-slip faults in granite. J Geophys Res Solid Earth 88:555–568
Serpa L, De Voogd B, Wright L, Willemin J, Oliver J, Hauser E, Troxel B (1988) Structure of the central Death Valley pull-apart basin and vicinity from COCORP profiles in the southern Great Basin. Geol Soc Am Bull 100:1437–1450
Sims D, Ferrill DA, Stamatakos JA (1999) Role of a ductile decollement in the development of pull-apart basins: experimental results and natural examples. J Struct Geol 21(5):533–554
Sneh A, Bartov Y, Weissbrod T, Rosensaft M (1998) Geological map of Israel, 1:200,000. Israel Geological Survey (4 sheets)
Sylvester AG, Smith RR (1976) Tectonic transpression and basement-controlled deformation in San Andreas fault zone, Salton Trough, California. AAPG Bull 57:74–96
Tchalenko JS (1970) Similarities between shear zones of different magnitudes. Geol Soc Am Bull 81:1625–1640
ten Brink US, Ben-Avraham Z, Bell RE, Hassouneh M Coleman, Andreasen DG, Tibor G, Coakley B (1993) Structure of the Dead Sea pull-apart basin from gravity analyses. J Geophys Res Solid Earth 98:21877–21894
Wetzler N, Sagy A, Sagy Y, Nahmias Y, Lyakhovsky V (2015) Active transform fault zone at the fringe of the Dead Sea basin. Tectonics 34(7):1475–1493
Woodcock NH, Fischer M (1986) Strike-slip duplexes. J Struct Geol 8(7):725–735
Ye J, Liu M, Wang H (2015) A numerical study of strike-slip bend formation with application to the Salton Sea pull-apart basin. Geophys Res Lett 42:1368–1374